Construction of sublimable pure organic ionic material with high solid luminescence efficiency based on anion-π^+ interactions tuning strategy

Kongqi Chen [a], Ganggang Li [a], Han Zhang [a], Haozhong Wu [a], Yin Li [a], Yuxuan Li [a], Zhiming Wang [a,*], Ben Zhong Tang [a,b,*]

[a] *AIE Institute, Center for Aggregation-Induced Emission, Key Laboratory of Luminescence from Molecular Aggregates of Guangdong Province, State Key Laboratory of Luminescent Materials and Devices, South China University of Technology, Guangzhou 510640, China*
[b] *Shenzhen Institute of Aggregate Science and Technology, School of Science and Engineering, The Chinese University of Hong Kong, Shenzhen, Guangdong 518172, China*

ARTICLE INFO

ABSTRACT

Charged species with π-conjugated moieties play a vital role in the development of organic electronic field, but the executable strategy of attaining high luminescent efficiency with sublimable pure organic salts is rare due to their inherent ionic nature and low vapor pressure, extremely restricting their application in the field of organic optoelectronics *via* common vacuum evaporation method. In this work, a series of central-type organic salts based polycyclic aromatic hydrocarbon (PAH) core are developed because of their potential higher luminescence efficiency than that of reported terminal-type organic salts like protonated pyridine framework, and they are equipped with aggregation-induced emission enhancement performance and tunable emission. The analyses of spectral data, crystal packing, and theoretical simulation demonstrate that rationally dispersing surface charge of large π cation by regulating donor–acceptor (D-A) distribution facilitates to increase anion-π^+ interactions and suppress the free rotation of phenyl groups, contributing to the fluorescence enhancement in the solid state. Notably, after tuning counter-ions' steric hindrance and dispersed charges ($BArF_{24}^-$), the sublimable pure organic ionic materials are obtained with high solid luminescence efficiency, and its vacuum-evaporated organic light-emitting diode (OLED) is prepared based on pure organic salt with bright yellow emission. Such inspiring results offer us new alternative material system for the organic optoelectronics.

1. Introduction

Aggregation-induced emission (AIE), regarded as an available means to achieve high solid luminescence efficiency, has obtained more and more attention due to their wide applications in the optical, electronic and optoelectronic field. [1–3] To better guide the design of molecules with AIE property, the most popular mechanisms, restriction of intramolecular motion (RIM), [4–5] have emerged, which is involved in noncovalent interactions. Among them, anion-π interactions are a class of important noncovalent interactions and play an important role in chemical and biological systems, [6–8] and they are unexplored for many years due to their instinctively repulsive nature. [9–11] Meanwhile, the positive charges are often found to participate in anion-π bonding to strengthen the binding ability, thus forming the anion-π^+ interactions. [12] Recently, employing anion-π^+ interactions successfully constructs AIE blocks, [13] offering us more possibilities to obtain

organic ionic material with high solid luminescence efficiency. Such organic ionic material attains a growing interest due to the tunable photophysical properties by varying both cation [14] and anion constituents. [15–18] The various counter-ions may not only positively affect their crystal packing, [19] resulting in enhanced emissive properties by reducing non-radiative decay channels, [13] but also influence the compound's photophysical properties owing to the electronic coupling within ionic pairs.

However, due to the unsatisfactory luminous efficiency and the lack of appropriate processing craft technology for such controllable organic salt compounds, the development of their optoelectronic characteristic has been extremely obstructed. [20] For the poor luminous efficiency, the reason lies in the relatively concentrated charge distribution for the most ionic molecules, leading to that charge can be served as traps and quench the emission. [21] For example, owing to their twisted structure for AIE compounds, the general AIE organic luminous ionic compounds,

whose anionic or cationic moieties are always located at separated aryl groups, such as pyridyl, furyl, and so on, and ionic feature become very local and centralized, usually exhibit unsatisfactory emission effect even though their solid luminous efficiency has been improved obviously. [22] As a result, such terminal-type organic salts might not be suitable to be as high-efficiency luminescence building blocks, and developing central-type organic salts becomes an effective alternative to solve the troublesome emission problem of ionic compounds. For the lack of processing craft technology, that is mainly attributed to the inherent ionic nature and low vapor pressure. [23]

Polycyclic aromatic hydrocarbons (PAHs), which are equipped with both semiconductor properties and clear and controllable chemical structure characteristics, have drawn tremendous attention owing to their unique optical, magnetic and electronic properties. [24–26] They are fused by sharing two adjacent carbon atoms consisting of sp^2 hybrid carbon centers, where the π electrons in PAHs can be delocalized in the whole conjugated system. [27] Furthermore, embedding heteroatoms such as boron, nitrogen, phosphorus, oxygen, or sulfur into the aromatic framework of PAHs can modulate their physical, structural and electronic properties, making them promising candidates for use in organic optoelectronic devices. [28–31] Owing to its pretty conjugation property and planarity, PAHs might be a reliable alternative to be developed a new kind of central-type ionic compounds with bright emission. Different from those reported terminal-type organic salts discussed above, [22] the charge distribution of the center-typed one based on PAHs was more easily tuned just by coordinating different electron-withdrawing or donating groups strength for obtaining better emission performance. Meanwhile, the anion effect could be magnified, and AIE behavior become easier to be tuned.

In this work, a series of benzo-fused azafluoranthenium salt derivatives based on PAHs salt reported before, [32] were prepared, and the donor–acceptor (D-A) strategy was introduced to regulate the surface distributions of electrostatic potential as shown in Scheme 1. In the meanwhile, the α_{AIE} ($\Phi_{F, film}$ / $\Phi_{F, soln.}$) of these derivatives was enhanced gradually after D-A modifcation and anion exchange. Owing to the large steric hindrance and well-dispersed charges for the large bulky volume anion (BArF$_{24}^-$), the high solid luminescence efficiency ionic material with sublimable property was successfully obtained. In addition, employed common vacuum-evaporated method in OLED preparation, this novel ionic emitter exhibited good performance with bright yellow emission. Hence, this work paves the way to develop a large class of novel pure organic ionic materials with AIE feature and high solid luminescence efficiency, offering the possibility to their applications in photoelectric devices.

2. Materials and methods

2.1. Chemicals and measurement

All the reagents and solvents were purchased from commercial sources and used as received. The final products were subjected to vacuum sublimation to further improve purity before photo-luminescence (PL) and electroluminescnce (EL) properties investigations. ^{1}H and ^{13}C NMR spectra were recorded on a Bruker AV 500 spectrometer. High resolution mass spectra (HRMS) were measured on a GCT premier CAB048 mass spectrometer operating in MALDI-TOF mode. Single crystal data were collected on Rigaku XtaLAB P2000 FR-X with a rotating copper anode and a Pilatus 200 K detector at room temperature. The structure was solved using intrinsic phasing and refined using least squares minimization. Thermogravimetric analysis (TGA) analysis was performed on a TA TGA Q5000 under dry nitrogen at a heating rate of 10 $^\circ$C min^{-1}. Cyclic voltammetry (CV) was performed on a CHI 610E A14297 in a solution of tetra-n-butylammonium hexafluorophosphate (Bu$_4$NPF$_6$) (0.1 M) in dichloromethane (DCM) or dimethylformamide (DMF) at a scan rate of 100 mV s^{-1}, using a platinum wire as the auxiliary electrode, a glass carbon disk as the working electrode and Ag/Ag$^+$ as the reference electrode. Ionization Potential (IP$_{CV}$) = [E$_{ox}$ − E$_{1/2}$(Fc/Fc$^+$) + 4.8] eV, Electron Affinities (EA$_{CV}$) = [E$_{red}$ − E$_{1/2}$(Fc/Fc$^+$) + 4.8] eV, where E$_{ox}$ and E$_{red}$ represent the onset oxidation potential and the reduction potential relative to Fc/Fc$^+$ (4.8 eV), respectively, and E$_{1/2}$ (Fc/Fc$^+$) represents the calibrated value. UV–vis absorption spectra were recorded with a Shimadzu UV-2600 spectrophotometer. Measurements of PL spectra were carried out on Horiba Fluoromax-4 spectrofluorometer. Fluorescence quantum yields in solutions and solid films were measured using a Hamamatsu absolute PL quantum yield spectrometer C11347 Quantaurus_QY. Fluorescence lifetimes were determined on a Hamamatsu C11367-11 Quantaurus-Tau time-resolved spectrometer. The Electron paramagnetic resonance (EPR) measurements were carried out on Bruker ELEXSYS-II E500 in X-band. The spectra were recorded at room temperature at a signal attenuation of 20 dB in quartz ESR standard quality tubes with an outer diameter of 5 mm from Beijing Synthware glass. All density functional theory (DFT) calculations were carried out using Gaussian 16 package for the geometry optimization and binding energy calculation based on M062X/6 − 31G (d, p) with long-range correction. The surface area distribution in different electrostatic potentials analysis was performed with Multiwfn 3.6 and VMD.

2.2. Synthesis and characterization

For compound PTC: Compound 1 was synthesized according the
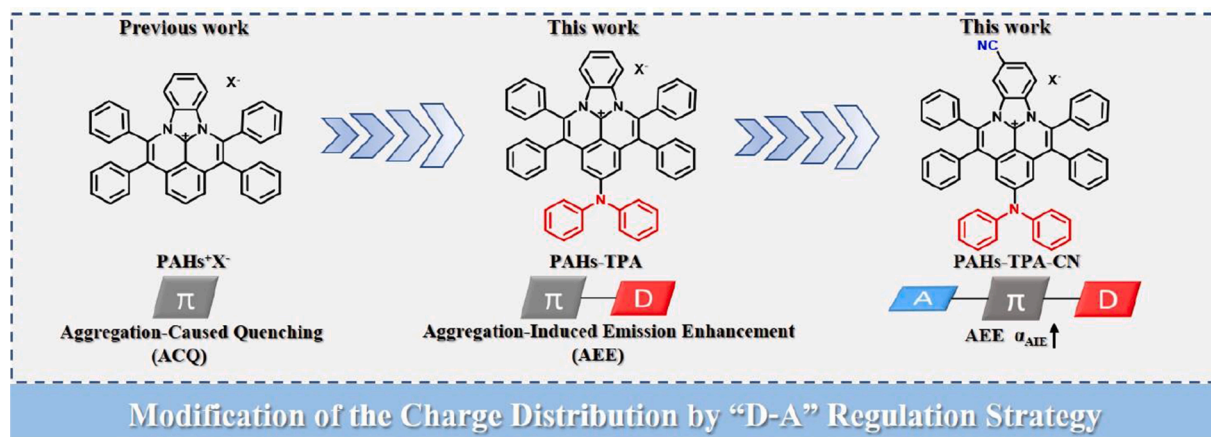
Scheme 1. Schematic illustration for the evolution of molecular design philosophy utilizing modification of the charge distribution by "D-A" regulation strategy; PAHs$^+$X$^-$ is from Ref 32 as a comparison; α_{AIE} is used as a factor or evaluation criteria to reflect AIE performance.

literature reported before. [33] A 50 mL sealed tube equipped with a magnetic stir bar, was charged with [RhCp*Cl$_2$]$_2$ (61.8 mg, 0.1 mmol, 2.5 mol %), 2-triphenylaminobenzimidazole (1) (1.45 g, 4.0 mmol, 100 mol %), diphenylacetylene (3) (1.43 g, 8.0 mmol, 200 mol %), AgOAc (2.79 g, 16.8 mmol, 420 mol %) and MeOH (20 mL). The reaction was heated at 100 °C for 5 h until disappearance of starting materials (TLC and/or ^{1}HNMR). The reaction mixture was quenched with NaCl(aq) solutions and extracted three times with DCM. Organic layers were dried over MgSO$_4$ and concentrated in vacuo. The residue was purified by flash column chromatography through an aluminum oxide pad using DCM / MeOH (49:1) as eluent to afford PTC as an earthy yellow solid in 85% yield (2.5 g, 3.4 mmol). ^{1}H NMR (500 MHz, DMSO-d_6) δ 7.65–7.53 (m, 10*H*), 7.39 (dd, *J* = 6.5, 3.3 Hz, 2H), 7.33 (d, *J* = 7.9 Hz, 4H), 7.28–7.12 (m, 16H), 6.79 (s, 2H), 6.13 (dd, *J* = 6.5, 3.3 Hz, 2H). ^{13}C NMR (126 MHz, DMSO-d_6) δ 153.89, 144.95, 137.76, 136.25, 134.82, 133.35, 131.48, 131.23, 131.01, 130.66, 130.50, 129.81, 129.45, 128.91, 128.55, 127.53, 126.70, 115.14, 111.62, 108.73. HRMS (MALDI-TOF): *m/z* (cation) 714.2963 [M$^+$, calcd 714.2904].

For compound PTP: A 25 mL round bottomed-flask was charged with silver hexafluorophosphate (100.7 mg, 0.4 mmol, 100 mol %), the compound PTC (300.1 mg, 0.4 mmol, 100 mol %) and DCM (5 mL) under argon atmosphere. The mixture was stirred at room temperature for 2 h until disappearance of starting material. The reaction mixture was filtered to eliminate AgCl residues and the solvent was evaporated in vacuo to afford the compound PTP as a yellow solid in 99% yield (340.5 mg, 0.396 mmol). ^{1}H NMR (400 MHz, DMSO-d_6) δ 7.65–7.54 (m, 10*H*), 7.38 (d, *J* = 9.7 Hz, 2H), 7.34 (t, *J* = 7.8 Hz, 4H), 7.29–7.13 (m, 16H), 6.78 (s, 2H), 6.13 (dd, *J* = 6.5, 3.3 Hz, 2H). ^{13}C NMR (101 MHz, DMSO-d_6) δ 144.95, 136.24, 134.81, 133.34, 131.46, 131.23, 131.00, 130.57, 129.81, 129.45, 128.91, 128.55, 127.53, 126.69, 115.14, 111.62. HRMS (MALDI-TOF): *m/z* (cation) 714.2967 [M$^+$, calcd 714.2904]; *m/z* (anion) 144.9727 [M$^-$, calcd 144.9647]. CCDC 2,089,249 contain the supplementary crystallographic data for this paper. These data can be obtained free of charge from The Cambridge Crystallographic Data Centre via www.ccdc.cam.ac.uk/data_request/cif.

For compound PTBF: A 25 mL round bottomed-flask was charged with sodium tetrakis(3,5-bis(trifluoromethyl)phenyl) borate (354.4 mg, 0.4 mmol, 100 mol %), the compound PTC (300.1 mg, 0.4 mmol, 100 mol %) and DCM (5 mL) under argon atmosphere. The mixture was stirred at room temperature for 2 h until disappearance of starting material. The reaction mixture was filtered to eliminate NaCl residues and the solvent was evaporated in vacuo to afford the compound PTBF as a merdoie solid in 99% yield (624.9 mg, 0.396 mmol). ^{1}H NMR (400 MHz, DMSO-d_6) δ 7.73 (s, 4H), 7.61 (dd, *J* = 11.8, 3.3 Hz, 18H), 7.42–7.31 (m, 6H), 7.30–7.12 (m, 16H), 6.79 (s, 2H), 6.13 (dd, *J* = 6.5, 3.3 Hz, 2H); ^{13}C NMR (126 MHz, DMSO-d_6) δ 162.00, 161.60, 161.20, 160.81, 153.89, 144.95, 137.76, 136.24, 134.81, 134.53, 133.34, 131.47, 131.22, 130.99, 130.65, 130.48, 129.81, 129.45, 128.90, 128.55, 127.74, 127.53, 126.69, 125.57, 123.40, 121.23, 118.24, 115.14, 111.63, 108.72. HRMS (MALDI-TOF): *m/z* (cation) 714.2889 [M+, calcd 714.2904]; *m/z* (anion) 863.0684 [M+, calcd 863.0654]. CCDC 2,089,255 contain the supplementary crystallographic data for this paper. These data can be obtained free of charge from The Cambridge Crystallographic Data Centre via www.ccdc.cam.ac.uk/data_request/cif.

For compound PTCNC: Compound 2 was synthesized according the literature reported before. [33] A 50 mL sealed tube equipped with a magnetic stir bar, was charged with [RhCp*Cl$_2$]$_2$ (61.8 mg, 0.1 mmol, 2.5 mol %), 2-triphenylamino-5-cyanobenzimidazole (2) (1.55 g, 4.0 mmol, 100 mol %), diphenylacetylene (3) (1.43 g, 8.0 mmol, 200 mol %), AgOAc (2.79 g, 16.8 mmol, 420 mol %) and MeOH (20 mL). The reaction was heated at 100 °C for 5 h until disappearance of starting materials (TLC and/or ^{1}HNMR). The reaction mixture was quenched with NaCl(aq) solutions and extracted three times with DCM. Organic layers were dried over MgSO$_4$ and concentrated in vacuo. The residue

was purified by flash column chromatography through an aluminum oxide pad using DCM / MeOH (49:1) as eluent to afford PTC as a yellow solid in 80% yield (2.48 g, 3.2 mmol). ^{1}H NMR (500 MHz, DMSO-d_6) δ 7.88 (dd, *J* = 9.0, 1.4 Hz, 1H), 7.71–7.56 (m, 10*H*), 7.35 (t, *J* = 7.9 Hz, 4H), 7.29–7.15 (m, 16H), 6.80 (dd, *J* = 4.4, 1.7 Hz, 2H), 6.21 (d, *J* = 9.0 Hz, 1H), 6.16 (d, *J* = 0.9 Hz, 1H); ^{13}C NMR (126 MHz, DMSO-d_6) δ 154.57, 144.65, 139.09, 135.97, 135.07, 132.96, 132.12, 131.50, 130.98, 130.60, 130.18, 130.00, 129.29, 128.99, 128.73, 128.23, 128.03, 126.93, 111.85, 111.61, 108.47, 108.12. HRMS (MALDI-TOF): *m/z* (cation) 739.2921 [M+, calcd 739.2862].

For compound PTCNP: A 25 mL round bottomed-flask was charged with silver hexafluorophosphate (100.7 mg, 0.4 mmol, 100 mol %), the compound PTCNC (310.2 mg, 0.4 mmol, 100 mol %) and DCM (5 mL) under argon atmosphere. The mixture was stirred at room temperature for 2 h until disappearance of starting material. The reaction mixture was filtered to eliminate AgCl residues and the solvent was evaporated in vacuo to afford the compound PTCNP as a yellow solid in 99% yield (350.2 mg, 0.396 mmol). ^{1}H NMR (400 MHz, DMSO-d_6) δ 7.88 (d, *J* = 9.0 Hz, 1H), 7.61 (dd, *J* = 13.4, 6.9 Hz, 10H), 7.34 (d, *J* = 7.4 Hz, 4H), 7.30–7.10 (m, 16H), 6.79 (s, 2H), 6.27–6.12 (m, 2H); ^{13}C NMR (101 MHz, DMSO-d_6) δ 154.57, 144.63, 139.11, 135.96, 135.05, 132.96, 132.10, 131.51, 130.93, 130.71, 130.63, 130.63, 129.77, 129.13, 128.77, 128.73, 128.23, 128.03, 126.93, 119.12, 117.95, 116.18, 108.50. HRMS (MALDI-TOF): *m/z* (catio) 739.2934 [M$^+$, calcd 739.2862]; *m/z* (anion) 144.9721 [M$^-$, calcd 144.9647].

For compound PTCNBF: A 25 mL round bottomed-flask was charged with sodium tetrakis(3,5-bis(trifluoromethyl)phenyl) borate (354.4 mg, 0.4 mmol, 100 mol %), the compound PTCNC (310.2 mg, 0.4 mmol, 100 mol %) and DCM (5 mL) under argon atmosphere. The mixture was stirred at room temperature for 2 h until disappearance of starting material. The reaction mixture was filtered to eliminate NaCl residues and the solvent was evaporated in vacuo to afford the compound PTCNBF as a merdoie solid in 99% yield (634.8 mg, 0.396 mmol). ^{1}H NMR (400 MHz, DMSO) δ 7.93 (d, *J* = 9.0 Hz, 1H), 7.74–7.61 (m, 22H), 7.39 (t, *J* = 7.7 Hz, 4H), 7.33–7.18 (m, 16H), 6.86 (d, *J* = 1.1 Hz, 2H), 6.31–6.21 (m, 2H); ^{13}C NMR (101 MHz, DMSO) δ 162.19, 161.69, 161.20, 160.70, 154.59, 144.65, 139.10, 135.96, 135.05, 134.52, 132.93, 132.10, 131.46, 130.94, 130.78, 130.35, 130.07, 129.51, 128.05, 126.88, 125.81, 123.10, 120.39, 119.12, 117.98, 116.18, 111.91, 108.54, 108.11. HRMS (MALDI-TOF): *m/z* (cation) 739.2940 [M$^+$, calcd 739.2862]; *m/z* (anion) 863.0747 [M$^-$, calcd 863.0654].

2.3. Device fabrication

The electroluminescence (EL) devices were fabricated by the vacuum-deposition method. Organic layers were deposited by high-vacuum (5×10^{-6} Torr) thermal evaporation onto a glass substrate pre-coated with an indium tin oxide (ITO) layer with a sheet resistance of 25 Ω square^{-1}. The organic films, LiF and aluminum were deposited according to the OLED configurations at deposition rates of $1 \sim 2$ Å s^{-1}, 0.1 Å s^{-1} and $3 \sim 5$ Å s^{-1}, respectively. The active area of each device was 3 mm × 3 mm. The EL spectra, the current density–voltage (*J-V*) characteristics and the current density–voltage-luminance (*J-V-L*) curves characterizations of the OLEDs were carried out with a Photo Research SpectraScan PR-745 Spectroradiometer and a Keithley 2450 Source Meter simultaneously. In the evaporation process, the evaporation rate and thickness are measured by quartz crystal oscillator, and then the actual thickness is measured by ellipsometer to calibrate the film thickness coefficient of quartz crystal oscillator. All measurements were done at room temperature under ambient conditions.

3. Results and discussion

3.1. Synthesis and characterization

As shown in Schemes S1 and S2, these polycyclic aromatic

hydrocarbons (PAHs) salts were readily synthesized *via* a facile one-step synthetic route reported previously, [32] which involved double C–H activation and annulation of 2-arylbenzimidazoles with alkynes under the catalysis of [RhCp*Cl$_2$]$_2$ and AgOAc with high yield. The detailed synthesis processes and structural characterization using high resolution mass spectroscopy (HRMS), ^{1}H NMR and ^{13}C NMR are provided in the supporting information (Figs. S1–S12). To better demonstrate and comprehend the properties of these compounds, we classify them into two families according to their central core difference, which can be named as PAHs-TPA derivatives (PTC, PTP, and PTBF) and PAHs-TPA-CN derivatives (PTCNC, PTCNP, and PTCNBF) shown in Fig. 1A. In addition, we observe these PAHs salts all exhibit excellent thermal stability from thermal gravimetric analysis. The decomposition temperature (T$_d$, corresponding to 5% weight loss) of these compounds are recorded at 420, 340, 389, 416, 264, 390 $^\circ$C for PTC, PTP, PTBF, PTCNC, PTCNP, and PTCNBF, respectively, and all of them exhibit good thermostability (Fig. S13).

3.2. Photophysical properties

As shown in Fig. 1B and Table 1, the UV – vis spectrum was measured in dimethyl sulfoxide (DMSO) solution with the absorption maximum at 382, 389, 389 nm for PAHs-TPA derivatives and at 397, 397, 400 nm for PAHs-TPA-CN derivatives. Upon photoexcitation, the green emission was detected at 529, 544, 544 nm for PAHs-TPA derivatives, while an obvious red-shift and weak yellow emission was observed for PAHs-TPA-CN derivatives compared to that of PAHs-TPA derivatives. Such phenomenon might be attributed to the stronger charge transfer (CT) ability for PAHs-TPA-CN derivatives compared to that of PAHs-TPA derivatives, which can be evidenced by the solvation effect, that is to say, with the same counter anion, the emissions of PAHs-TPA-CN derivatives are more red-shifted than that of PAHs-TPA-CN derivatives with the change of solvent polarities (Fig. S14). It's worth noting that not only the absorption but also the PL emissions were identical in PTP and PTBF solutions, and the same phenomenon in PTCNC and PTCNP solutions was also observed, demonstrating that it is the large π conjugated cation that mainly contributes to the luminescence in solutions. As for PTC and PTCNBF, however, they had a blue-

shift and red-shift respectively compared to their corresponding other PAHs-TPA derivatives and PAHs-TPA-CN derivatives, which might be caused by inductive effect of the counter anion. Thus, the blue-shift of the former and the red-shift of the latter demonstrated that the inductive effect of BArF$_{24}$$^-$ was stronger than that in Cl$^-$. Comparing their PL emissions in solutions and in the film (Fig. 1C-D), we could find these compounds exhibited aggregation-induced blue-shifted emission (AIBSE) characteristics, which was attributed to the lower reorganization energies in aggregates than in the solution phase. [34] And such AIBSE phenomenon could be vividly observed under 365 nm UV illumination from a hand-held UV lamp (Fig. S17). The absolute quantum yield (Φ_F) values of PTC, PTP, PTBF, PTCNC, PTCNP and PTCNBF in DMSO were tested to be 15.8%, 30.7%, 27.8%, 4.5%, 7.2% and 7.8%, respectively. After fabricated into solid films, PAHs-TPA derivatives displayed a slightly increased Φ_F of 30.7%, 42.4% and 52.6%, respectively, while PAHs-TPA-CN derivatives showed an obviously relative ascending Φ_F of 21.5%, 46.8% and 62.8%, respectively, indicating that the two kinds of PAHs derivatives possessed aggregation-induced emission enhancement property and α_{AIE} gradually increased with change of both cation and anion. And such feature could be confirmed by the photoluminescence (PL) spectra of these compounds measured in DMSO and water mixed solutions in Fig. 1E, Fig. S15 and S16.

For a comprehensive investigation, the lifetime was also measured in pure DMSO and in the solid state, coupled with the quantum yield (QY), the molecular dynamics of the excited states were investigated to make out the fluorescence enhancement in aggregates. As shown in Table 1, the radiative decay rate (k_r) of these PAHs-TPA derivatives increased from $2.32 \times 10^7 \mathrm{s}^{-1} \sim 4.46 \times 10^7 \mathrm{s}^{-1}$ in solution to $6.57 \times 10^7 \mathrm{s}^{-1} \sim 14.82 \times 10^7 \mathrm{s}^{-1}$ in the film, and the nonradiative decay rate (k_{nr}) exhibited the similar tendency with the values from $9.85 \sim 12.34 \times 10^7$ in solution to $13.35 \sim 14.84 \times 10^7 \mathrm{s}^{-1}$ in films. By contrast, the radiative decay rate was increased a lot but the nonradiative decay rate got extremely suppressed in the film for PAHs-TPA-CN derivatives. Clearly, it is only the improvement of radiative channel that accounts for the relatively small α_{AIE} for PAHs-TPA derivatives, while the synergistic effect of the promotional radiative channel and the suppressed nonradiative channel results in the larger α_{AIE} for PAHs-TPA-CN derivatives. Taking all discussed above into consideration, we could find that simply
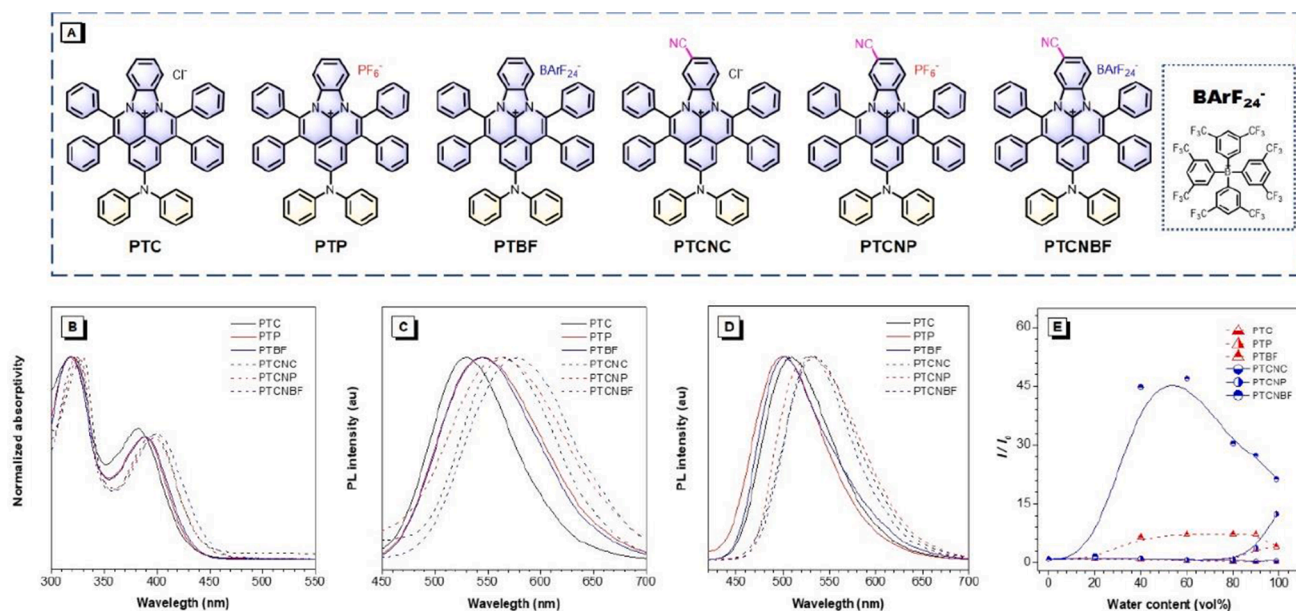
Fig. 1. (A) Molecular structures the PAHs-TPA derivatives (PTC, PTP and PTBF) and PAHs-TPA-CN derivatives (PTCNC, PTCNP and PTCNBF). Photophysical properties of the molecules. (B) UV spectra and photoluminescence (PL) spectra of PTC, PTP, PTBF, PTCNC, PTCNP, and PTCNBF (10 μM) in DMSO solution (C) and in the films (D). (E) Plot of relative fluorescence intensity (I / I_0) versus different water fractions for PTC, PTP, PTBF, PTCNC, PTCNP, and PTCNBF. Concentration: 10 μM.

Table 1
Photophysical properties of PAHs-TPA derivatives and PAHs-TPA-CN derivatives.

Compounds	λ_{abs}[(a)] (nm)	λ_{em} (nm)		Φ_F(%)			α_{AIE}[(b)]	τ (ns)		k_r ($10^7 s^{-1}$)[(c)]		k_{nr} ($10^7 s^{-1}$)[(d)]	
		soln[(a)]	film	soln[(a)]	powder	film		soln[(a)]	film	soln	film	soln	film
PTC	382	529	507	15.8	7.5	30.7	1.94	6.82	4.67	2.32	6.57	12.34	14.84
PTP	389	544	500	30.7	32.6	42.4	1.38	6.89	4.26	4.46	9.95	10.05	13.52
PTBF	389	544	501	27.8	64.9	52.6	1.89	7.33	3.55	3.79	14.82	9.85	13.35
PTCNC	397	567	534	4.5	29.8	21.5	4.78	6.82	2.28	0.66	9.43	14.0	34.43
PTCNP	397	567	528	7.2	31.5	46.8	6.50	2.06	4.37	3.50	10.72	45.04	12.16
PTCNBF	400	577	529	7.8	78.6	62.8	8.05	2.98	4.05	2.62	15.51	30.93	9.18

measured in DMSO solution. [(b)] $\alpha_{AIE} = \Phi_{F,\,film} / \Phi_{F,\,soln}$. [(c)] k_r = radiative decay rate (Φ_F/τ). [(d)] k_{nr} = nonradiative decay rate ($1/\tau - k_r$). Abbreviation: λ_{abs} = maximum absorption wavelength; λ_{em} = maximum emission wavelength; Φ_F = absolute quantum yield; τ = life time; k_r = radiative decay rate; k_{nr} = nonradiative decay rate.

modifying the structure of large planar cation will affect obviously the optical properties.

3.3. Theoretical calculation

To further understand the different photophysical properties among these PAHs salt derivatives, the density functional theory calculations were performed at the basis set of M06-2X/6-31G** *via* Gaussian 09. As shown in Fig. S18, almost propeller conformations of diphenyl-ethyleneyl group were observed among them, which would lead to a larger spatial structure for suppressing detrimental π-π stacking. And the optimized structures of PAHs-TPA and PAHs-TPA-CN (removing the counterions) had similar large torsion angles between surrounding four freely rotating phenyl groups and polycyclic arenes salt plane about 67°-76°, leading to no distributions of electron clouds on them. As depicted in Fig. S18, their highest occupied molecular orbitals (HOMOs) mainly located at the triphenylamine (TPA) moiety. Owing to the introduction of the cyano-group into PAHs-TPA-CN, these two kinds of PAHs salts showed different electron clouds distributions in the lowest unoccupied molecular orbitals (LUMOs), which was contributed by the orbitals from

the polycyclic arenes salt plane and cyano-group for PAHs-TPA-CN but only the polycyclic arenes salt plane for PAHs-TPA. Obviously, PAHs-TPA-CN exhibited larger separated charge distribution than that of PAHs-TPA, indicating that PAHs-TPA-CN has the stronger CT capability and it is in accord with its red-shifted and weaker emission in solutions compared to that of PAHs-TPA discussed above.

It is well-known that the electrostatic potential (ESP) of molecular van der Waals surface is closely related to the characteristics of inter-molecular interaction, [35–36] which is beneficial for us to comprehend their photoluminescence behavior. Fig. 2C and D displayed the structure and molecular ESP surface of PAHs-TPA and PAHs-TPA-CN, respectively. Compared with PAHs-TPA, the surface area distribution in different electrostatic potential regions of PAHs-TPA-CN was more centralized but the electrostatic potential regions were relatively more scattered (Fig. 2A and B), which contributes to the more possibilities for PAHs-TPA-CN to interact with the counterion or adjacent molecule. Further investigation of the optimized structures of PTC, PTP, PTCNC and PTCNP found that anion-π+ interactions with distances of 2.926, 3.783, 2.918 and 3.625 Å and energies of −84.28, −81.46, −88.63 and −85.91 kcal·mol⁻¹ were observed between the chlorine or fluorine
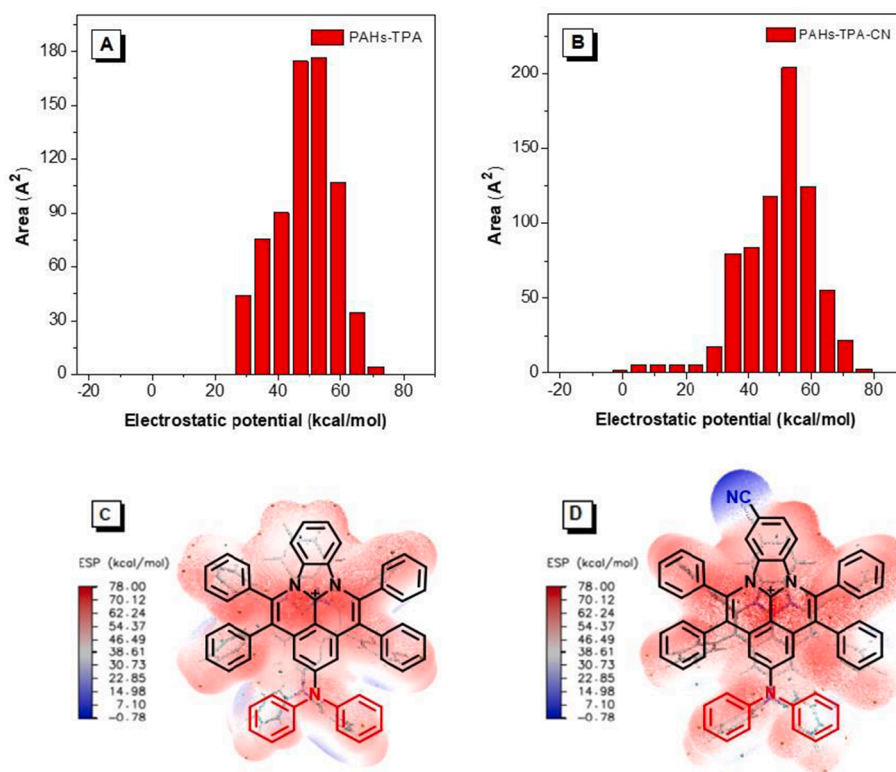
Fig. 2. Surface area distribution in different electrostatic potentials of (A) PAHs-TPA (removing counterions) and (B) PAHs-TPA-CN (removing counterions). ESP surface and molecule structures of PAHs-TPA (C) and PAHs-TPA-CN (D).

atoms of hexafluorophosphate anions and the positively-charged imidazole core (Fig. 3). Thus, the anion-π^+ interactions of the PAHs-TPA-CN derivatives were stronger than that of PAHs-TPA derivatives and such strong anion-π^+ interactions efficiently impeded the π-π stacking to avoid emission quenching, which accounted for the larger value of α_{AIE} for PAHs-TPA-CN derivatives. Taking the discussion above into consideration, we could easily acknowledge that the rational attachment different electron-donating/electron-withdrawing groups to the electron-deficient cation core can coordinate the distribution of electrostatic potential of molecular van der Waals surface, thus adjusting the interaction between the luminescent large π cation and anion to achieve aggregation-induced emission enhancement property.

3.4. Crystal structures

Single crystals of PTP and PTBF were successfully obtained in petroleum ether/dichloromethane (DCM) mixtures by slow solvent evaporation, which could confirm their molecular structures and configurations. As a whole, the luminous large conjugated π cation exhibited twisted propeller conformation, leading to less π-π stacking interactions and suppressing aggregation-caused fluorescence quenching to some extent. To better specifically unveil the different photoluminescence behaviors among these compounds with different counter anion, we carefully analyzed their crystal stacking patterns, which provided direct evidence for such discrepancy. As shown in Fig. 4A, PTP showed a typical indented stacking and the layers were punctuated by PF_6^-, extremely extending the distances of the intermolecular π-π interactions. By comparison, owing to the introduction of more voluminous $BArF_{24}^-$ anion, the PTBF exhibited irregular packed model and no π-π interactions were observed (Fig. 4D). Notably, obvious anion-π^+ interactions between the fluorine atoms of anions and the positively charged PAHs core were found both in these two crystals (Fig. 4C and F). Meanwhile, intramolecular and intermolecular F-H hydrogen bonds were also observed in the crystal lattice, which contributes to constraining rotation of the phenyl rings effectively and thereby rigidifies the structure of the crystal lattice (Fig. 4B and E). It is such different F-H hydrogen bond interactions in these two crystals that caused their different optical phenomenon. Specifically, more F-H hydrogen bond interactions in the PTBF crystal lattice were found than that in PTP, and

almost all freely rotating phenyl groups were restricted in PTBF compared with that in PTP, contributing to the higher quantum yield of PTBF. Such result reveals the substitution of larger bulky volume anion might be an efficient means to achieve high solid luminescence efficiency for such PAHs salt.

3.5. EPR studies

Interestingly, PAHs salts with small bulky volume anion (Cl^- and PF_6^-) showed very low quantum yield in powders compared to that in films. Considering that there may exist incomplete charge transfer between the large π cation and counterions in compact stacking mode, we conducted electron paramagnetic resonance (EPR) experiment to confirm whether there exist radical species. As shown in Fig. 5, all these PAHs salts exhibited positive paramagnetic response, revealing the formation of radical in powders. Furthermore, the intensities of EPR signals were synergistically affected by the counterions, that is to say, the intensities gradually decreased after the substitution of larger bulky volume anion, because the larger size of counterions would weaken the strength of PAHs-X$^-$ (X = Cl, PF_6, and $BArF_{24}$) ionic bonds and result in more separable anions. [23] Aside from the inductive effect of the counterions, the influence caused by variation of the substituent groups of the PAHs backbones were more pronounced. As shown in Fig. 5A and B, the EPR intensity of PTCNC was weaker than that of PTC, demonstrating that substituents with both electron-donating feature could stabilize the radical to some extent. Noticeably, the luminous efficiency has the opposite tendency to the intensities of EPR signals (Fig. 5C), which might be attributed to the radical-enhanced intersystem crossing (EISC) effect, [37–39] thus leading to the decrease of exciton of radiative transition. Such results further indirectly prove that the introduction of donor–acceptor (D-A) system exactly make a difference to the charge distribution.

3.6. Sublimation property

It is reported that anionic volume of $BArF_{24}^-$ is 425.02 cm^3 mol^{-1} much larger than that of PF_6^- (49.95 cm^3 mol^{-1}) and positive charges on the boron centers of $BArF_{24}^-$ is only 0.18 much lower than that on the phosphorus center of PF_6^- (as high as 1.25). [23] As a result, the
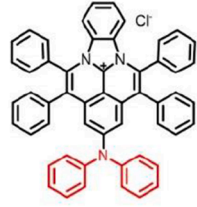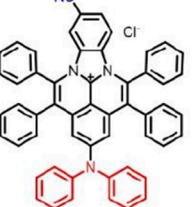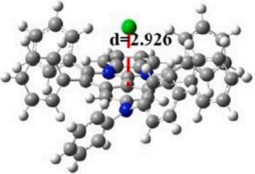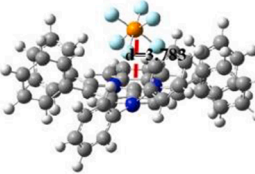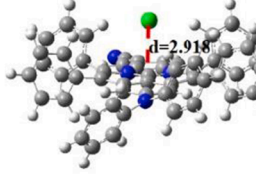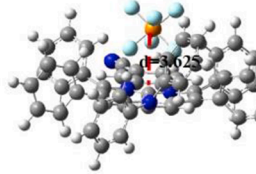

Fig. 3. Molecular, optimized structures and binding energy for PTC, PTP, PTCNC, and PTCNP. Calculations were performed by density functional theory calculations at the M06-2X/6-31G** level using the Gaussian 09 program. Hydrogen, carbon, nitrogen, chlorine, fluorine and phosphorus were shown in white, gray, blue, green, sky blue and orange, respectively.
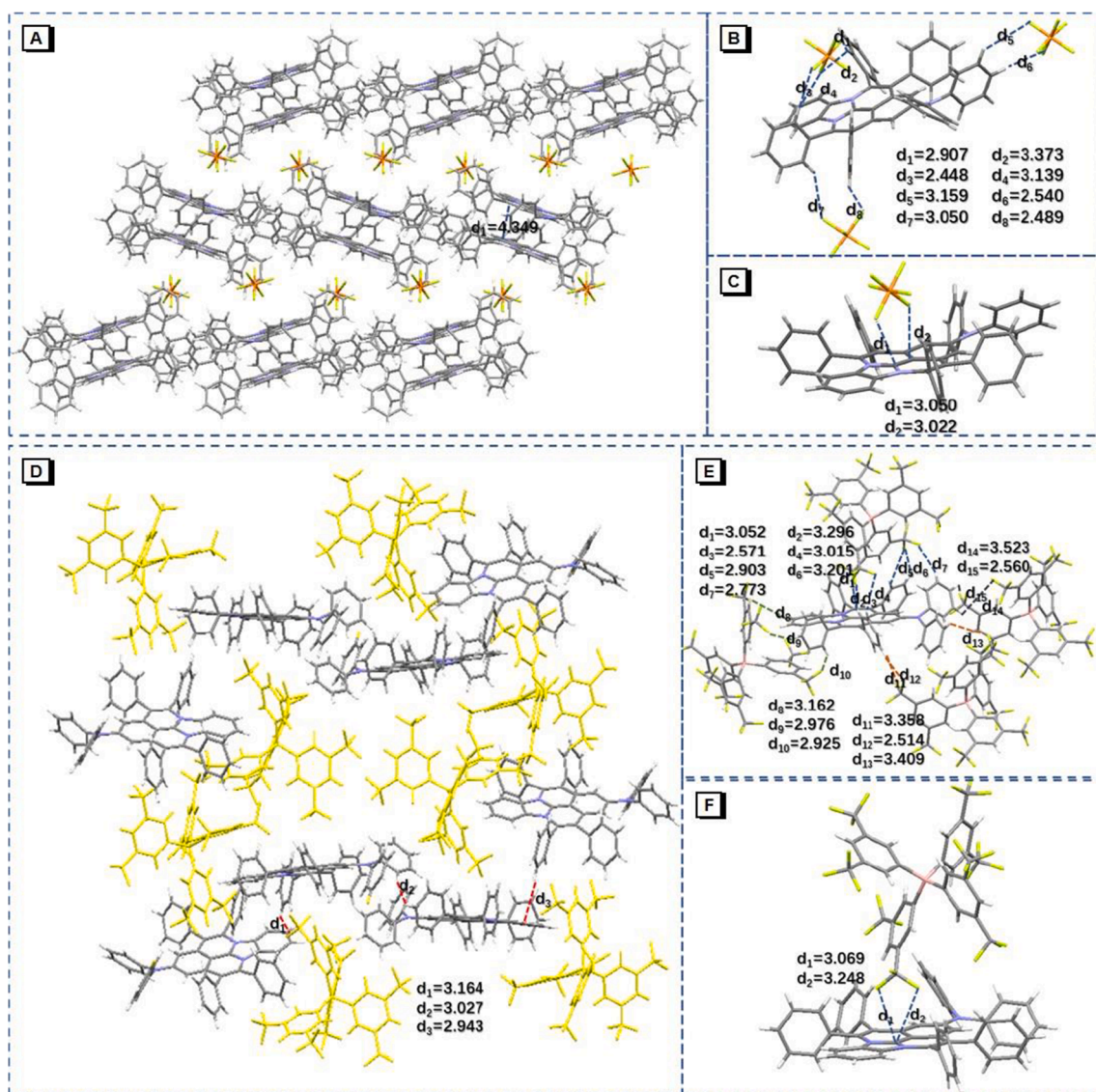
Fig. 4. Stacking mode in single crystal structure of PTP (A) and PTBF (D); intramolecular hydrogen bonding interactions in the single crystal structure of PTP (B) and PTBF (E). F-H interactions among anion-π + n the single crystal structure of PTP (C) and PTBF (F).
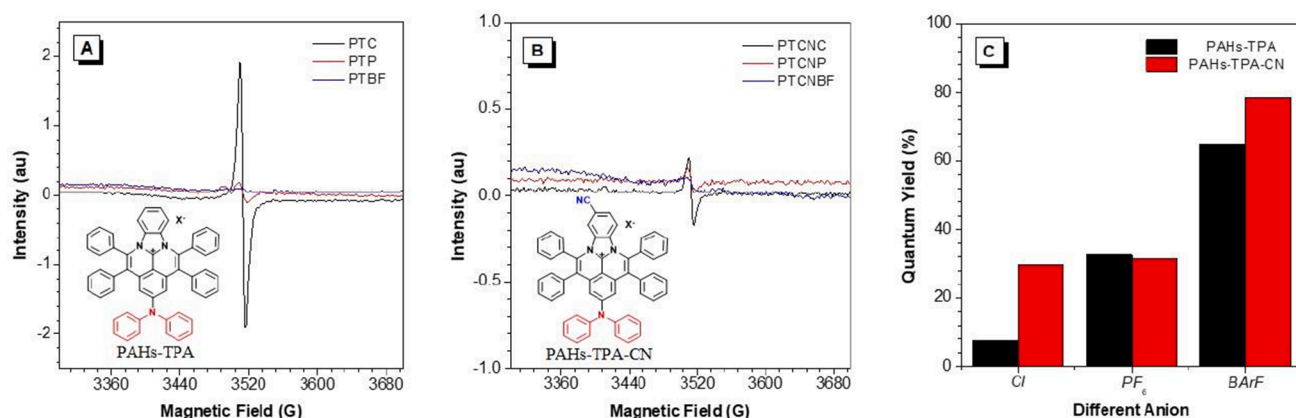

Fig. 5. EPR spectra of studied PAHs salts with varied counterions for PAHs-TPA derivatives (A) and PAHs-TPA-CN derivatives (B). And quantum yield for PAHs salts with varied counterions in powders (C).

distances between the center of positively-charged imidazole core and boron exceed 8 Å as shown in Fig. S19, quite larger than that between the center of positively-charged imidazole core and phosphorus (about 4 Å). Therefore, owing to the large steric hindrance and well-dispersed charges for $BArF_{24}^{-}$, PTBF and PTCNBF, whose longer ionic radii results in weaker lattice energies and electrostatic interaction, have the possibility to achieve sublimable ionic materials. Delightedly, the structures of PTBF and PTCNBF didn't change at all before and after sublimation (Fig. S20 and S21), indicating that the introduction of large bulky counterions could indeed improve its volatility and achieve the sublimation for pure organic salts.

3.7. Vacuum-Evaporated properties verification in OLEDs

Encouraged by the sublimable property of PTBF and PTCNBF, we take PTCNBF as an example to try to fabricate vacuum-deposited OLEDs thereof and evaluated their performance. Previously, the electrochemical property of PTCNBF was investigated by cyclic voltammetry (CV). On the basis of their oxidation and reduction onsets against Fc/Fc^{+} redox couple (Fig. S22), the ionization potential value (IPCV) of PTCNBF is estimated to be 5.92 eV, while the value of electron affinities (EACV) is approximate to be 3.10 eV. Subsequently, we employed the PTCNBF as emitting layers (EML) with different thickness to fabricate nondoped OLEDs (devices I − III) with a configuration of ITO (indium tin oxide)/ HATCN (5 nm)/NPB (40 nm)/TCTA (5 nm)/EML (20/30/40 nm)/ TmPyPB (40 nm)/LiF (1 nm)/Al (120 nm) (Fig. 6A), where 1,4,5,8,9,11-hexaazatriphenylene-hexacarbonitrile (HATCN), N,N'-Bis- (1-naphthalenyl)-N,N'-bis-phenyl-(1,1′-biphenyl)-4,4′-diamine (NPB), tris(4-carbazoyl-9-ylphenyl)amine (TCTA), 1,3,5-tri(m-pyridin-3-ylphenyl) benzene (TmPyPB), and LiF functioned as the hole injection, hole-transporting, exciton-blocking, electron-transporting, and electro-injection layers, respectively. [40]

Table 2

EL performances of the nondoped OLEDs based on the PTCNBF.

Device[a]	λ_{EL} (nm)	V_{on} (V)	L (cd/ m^2)	η_c (cd/ A)	η_p (lm/ W)	EQE_{max} (%)	CIE (x, y)
I	536	4.4	58	8.76	6.26	3.35%	(0.357, 0.570)
II	538	4.4	65	14.78	10.55	4.54%	(0.374, 0.581)
III	544	4.8	47	14.88	8.66	4.82%	(0.393, 0571)

[a]Abbreviation: EML = Emission layer; λ_{EL} = EL maximum at 10 mA cm^{-2}; V_{on} = turn-on voltage at 1 cd m^{-2}; L = maximum luminance; η_c = maximum current efficiency; η_p = maximum power efficiency; EQE_{max} = maximum external quantum efficiency; CIE = Commission Internationale de L 'Eclairage, recorded at 10 mA cm^{-2}.

The optimized device performance is summarized in Table 2. The devices were turned on at low voltages of 4.4–4.8 V, and emitted yellow light with corresponding EL peaks at 536, 538, and 544 nm for these three groups of devices with different thickness emitting layers (EML) at 20, 30, 40 nm, respectively (Fig. 6B). The EL spectra resemble their PL spectra in neat films, suggesting that in these devices, most excitons were electrogenerated in the light-emitting layer. However, the maximum luminance (L_{max}) was only 47 ∼ 68 cd m^{-2} (Fig. 6C), which might be attributed to the capture effect to exciton from inherent ionic feature. In addition, we could find the maximum η_{ext} values of the nondoped OLEDs gradually increased from 3.35% to 4.82% with the increasement of EML thickness (Fig. 6D). Thus, the increase in thickness could relatively dilute the exciton concentration and reduce the exciton quenching chance from ionic trap. And the similar consequence could also be achieved in the OLEDs doped with 20 wt% 4,4′-bis(N-
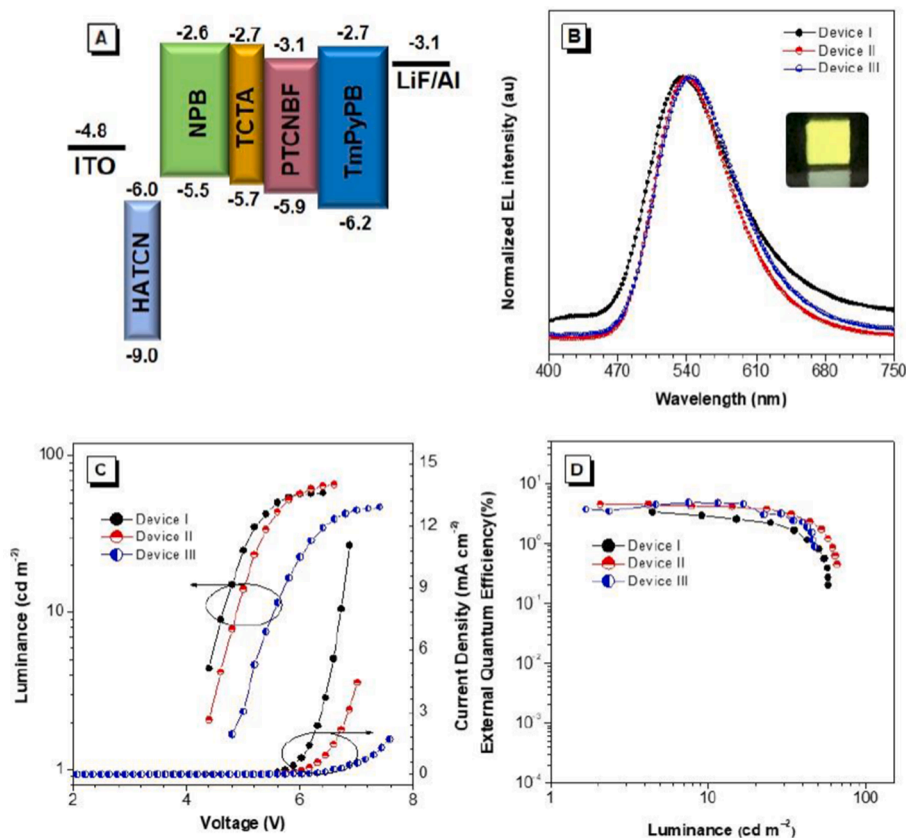
Fig. 6. (A) Device structure, (B) EL spectra, (C) current density–voltage–luminance (*J–V–L*) characteristics, and (D) external quantum efficiency versus luminance curves of the nondoped OLEDs based on the PTCNBF.

carbazolyl)-1,1′-biphenyl (CBP) or 2,8-bis (diphenylphosphine oxide) dibenzofuran (PPF) (Fig. S23 and Table S1), further indirectly confirming that ionic charge could devitalize exciton to some extent. But even so, it is worth noting that purification of ionic material by sublimation plays an important role in maximize its photoelectric performance and vacuum-evaporated craft can keep the film uniformity, which will prompt the development of such organic salt material in the appication of special optoelectronic devices.

4. Conclusion

In summary, a series of large π cationic central-typed PAHs salts with different counterions were synthesized and fully characterized. These derivatives all presented aggregation-induced emission enhancement property and were equipped with tuning α_{AIE} by adjusting central charge distribution through D-A regulation strategy. The theoretical simulations and photophysical measurements all elucidated that the introduction of CN group could enlarge the CT ability and disperse the surface area distribution in different electrostatic potential, resulting in weaker emission in solutions and stronger anion-π^+ interactions for PAHs-TPA-CN derivatives than that of PAHs-TPA derivatives. The analysis of single crystal all revealed that large bulky volume anion ($BArF_{24}^-$) could more efficiently block the detrimental π-π stacking and suppress the rotation of surrounding phenyl groups compared to small volume anion (PF_6^- and Cl^-), successfully achieving the high solid luminescence efficiency with 78.6 % for PTCNBF. Otherwise, the sublimable pure organic luminescent ionic materials were obtained resoundingly through counter-ion control. Using such novel organic ionic emitters with high brightness, PTCNBF, we succeed in the preparation of efficient vacuum-evaporated OLED with relatively good performance. Thus, our findings may offer a possible solution to understand thermodynamic mechanisms of vacuum evaporation deposition and provide a powerful tool to develop novel material systems to extend the device performance even beyond that reported here.

Declaration of Competing Interest

The authors declare that they have no known competing financial interests or personal relationships that could have appeared to influence the work reported in this paper.

Acknowledgements

Appendix A. Supplementary data

Supplementary data to this article can be found online at https://doi.org/10.1016/j.cej.2021.133646.

References

[1] J. Mei, N.L. Leung, R.T. Kwok, J.W. Lam, B.Z. Tang, Aggregation-induced emission: together we shine, united we soar!, Chem. Rev. 115 (2015) 11718–11940.

[2] R.T.K. Kwok, C.W.T. Leung, J.W.Y. Lam, B.Z. Tang, Biosensing by luminogens with aggregation-induced emission characteristics, Chem. Soc. Rev. 44 (13) (2015) 4228–4238.

[3] J. Yang, M. Fang, Z. Li, Organic luminescent materials: the concentration on aggregates from aggregation-induced emission, Aggregate 1 (2020) 6–18.

[4] N.L.C. Leung, N. Xie, W. Yuan, Y. Liu, Q. Wu, Q. Peng, Q. Miao, J.W.Y. Lam, B. Z. Tang, Restriction of intramolecular motions: the general mechanism behind aggregation-induced emission, Chem. Eur. J. 20 (2014) 15349–15353.

[5] M.-H. Jiang, S.-K. Li, X. Zhong, W.-B. Liang, Y.-Q. Chai, Y. Zhuo, R. Yuan, Electrochemiluminescence enhanced by restriction of intramolecular motions (RIM): tetra phenylethylene microcrystals as a novel emitter for mucin 1 detection, Anal. Chem. 91 (2019) 3710–3716.

[6] C. Estarellas, A. Frontera, D. Quiñonero, P.M. Deyà, Relevant anion-π interactions in biological systems: the case of urate oxidase, Angew. Chem., Int. Ed. 50 (2) (2011) 415–418.

[7] M.J. Langton, C.J. Serpell, P.D. Beer, Anion recognition in water: recent advances from a supramolecular and macromolecular perspective, Angew. Chem., Int. Ed. 55 (2016) 1974–1987.

[8] D.-X. Wang, M.-X. Wang, Exploring Anion-π interactions and their applications in supramolecular chemistry, Acc. Chem. Res. 53 (7) (2020) 1364–1380.

[9] J. Zhang, L. Xiang, B. Yan, H. Zeng, Nanomechanics of anion-π interaction in aqueous solution, J. Am. Chem. Soc. 142 (2020) 1710–1714.

[10] M. Giese, M. Albrecht, K. Rissanen, Experimental investigation of anion-π interactions–applications and biochemical relevance, Chem. Commun. 52 (9) (2016) 1778–1795.

[11] H.T. Chifotides, K.R. Dunbar, Anion-π interactions in supramolecular architectures, Acc. Chem. Res. 46 (4) (2013) 894–906.

[12] A. Frontera, P. Gamez, M. Mascal, T.J. Mooibroek, J. Reedijk, Putting anion–π interactions into perspective, Angew. Chem., Int. Ed. 50 (41) (2011) 9564–9583.

[13] J. Wang, X. Gu, P. Zhang, X. Huang, X. Zheng, M. Chen, H. Feng, R.T.K. Kwok, J.W. Y. Lam, B.Z. Tang, Ionization and anion-π^+ interaction: a new strategy for structural design of aggregation-induced emission luminogens, J. Am. Chem. Soc. 139 (2017) 16974–16979.

[14] Z. Cheng, H. Shi, H. Ma, L. Bian, Q.i. Wu, L. Gu, S. Cai, X. Wang, W.-W. Xiong, Z. An, W. Huang, Ultralong phosphorescence from organic ionic crystals under ambient conditions, Angew. Chem., Int. Ed. 57 (3) (2018) 678–682.

[15] Kenry, C. Chen, B. Liu, Enhancing the performance of pure organic room-temperature phosphorescent luminophores, Nat. Commun. 10 (1) (2019), https://doi.org/10.1038/s41467-019-10033-2.

[16] E. Lucenti, A. Forni, C. Botta, L. Carlucci, C. Giannini, D. Marinotto, A. Pavanello, A. Previtali, S. Righetto, E. Cariati, Cyclic triimidazole derivatives: intriguing examples of multiple emissions and ultralong phosphorescence at room temperature, Angew. Chem., Int. Ed. 56 (2017) 16302–16307.

[17] W. Zhao, Z. He, J.Y. Lam, Q. Peng, H. Ma, Z. Shuai, G. Bai, J. Hao, B. Tang, Rational molecular design for achieving persistent and efficient pure organic room-temperature phosphorescence, Chem 1 (4) (2016) 592–602.

[18] P. Alam, N.L.C. Leung, J. Liu, T.S. Cheung, X. Zhang, Z. He, R.T.K. Kwok, J.W. Y. Lam, H.H.Y. Sung, I.D. Williams, C.C.S. Chan, K.S. Wong, Q. Peng, B.Z. Tang, Two are better than one: a design principle for ultralong-persistent luminescence of pure organics, Adv. Mater. 32 (2020) 2001026.

[19] G. Zhang, X. Zhang, L. Kong, S. Wang, Y. Tian, X. Tao, J. Yang, Anion-controlled dimer distance induced unique solid-state fluorescence of cyano substituted styrene pyridinium, Sci. Rep. 6 (2016) 37609.

[20] H. Xu, R. Meng, C. Xu, J. Zhang, G. He, Y. Cui, A monolayer organic light-emitting diode using an organic dye salt, Appl. Phys. Lett. 83 (2003) 1020–1022.

[21] M. Martini, F. Meinardi, A. Vedda, The role of alkali ions in the 190 K TSL peak in quartz, Radiat. Meas. 32 (2000) 673–677.

[22] Y.H. Zhang, X. Li, L. Huang, H.S. Kim, J. An, M. Lan, Q.Y. Cao, J.S. Kim, AIE based GSH activatable photosensitizer for imaging-guided photodynamic therapy, Chem. Commun. 56 (2020) 10317–10320.

[23] D. Ma, Y. Qiu, L. Duan, New insights into tunable volatility of ionic materials through counter-ion control, Adv. Funct. Mater. 26 (20) (2016) 3438–3445.

[24] M. Stępień, E. Gońka, M. Żyła, N. Sprutta, Heterocyclic nanographenes and other polycyclic heteroaromatic compounds: synthetic routes, properties, and applications, Chem. Rev. 117 (2017) 3479–3716.

[25] M. Hirai, N. Tanaka, M. Sakai, S. Yamaguchi, Structurally constrained boron-, nitrogen-, silicon-, and phosphorus-centered polycyclic π-conjugated systems, Chem. Rev. 2019 (119) (2019) 8291–8331.

[26] C. Zeng, B. Wang, H. Zhang, M. Sun, L. Huang, Y. Gu, Z. Qiu, K. Müllen, C. Gu, Y. Ma, Electrochemical synthesis, deposition, and doping of polycyclic aromatic hydrocarbon films, J. Am. Chem. Soc. 143 (7) (2021) 2682–2687.

[27] J. Wu, W. Pisula, K. Müllen, Graphenes as potential material for electronics, Chem. Rev. 107 (3) (2007) 718–747.

[28] C.-W. Ju, B.o. Li, L. Li, W. Yan, C. Cui, X. Ma, D. Zhao, Modular synthesis of pentagonal and hexagonal ring-fused NBN-phenalenes leading to an excited-state aromatization-induced structural planarization molecular library, J. Am. Chem. Soc. 143 (15) (2021) 5903–5916.

[29] V.M. Hertz, M. Bolte, H.-W. Lerner, M. Wagner, Boron-containing polycyclic aromatic hydrocarbons: facile synthesis of stable, redox-active luminophores, Angew. Chem., Int. Ed. 54 (2015) 8924–8928.

[30] Y. Deng, Y. Xie, K. Zou, X. Ji, Review on recent advances in nitrogen-doped carbons: preparations and applications in supercapacitors, J. Mater. Chem. A 4 (2016) 1144–1173.

[31] H. Huang, D. Chen, F. Li, Z. Xing, J. Zhao, D. Wu, G. Liang, J. Xia, BN-embedded eleven-ring fused heteroaromatics: Synthesis, optoelectronic properties and fluoride susceptibility, Dyes Pigments 177 (2020), 108271.

[32] J.M. Villar, J. Suárez, J.A. Varela, C. Saá, N-Doped cationic PAHs by Rh (III)-catalyzed double C-H activation and annulation of 2-arylbenzimidazoles with alkynes, Org. Lett. 19 (7) (2017) 1702–1705.

[33] J. Pina, J.S. Seixas de Melo, R.M. Batista, S.P. Costa, M.M.M. Raposo, Triphenylamine-benzimidazole derivatives: synthesis, excited-state characterization, and DFT studies, J. Org. Chem. 78 (2013) 11389–11395.

[34] Y. Chandrasekaran, N. Venkatramaiah, S. Patil, Tetraphenylethene-based conjugated fluoranthene: a potential fluorescent probe for detection of nitroaromatic compounds, Chem. Eur. J. 22 (2016) 5288–5294.

[35] R. Pollice, P. Chen, A universal quantitative descriptor of the dispersion interaction potential, Angew. Chem. Int. Ed. 58 (29) (2019) 9758–9769.

[36] K. Kumara, A.D. Kumar, S. Naveen, K.A. Kumar, N.K. Lokanath, Synthesis, spectral characterization and X-ray crystal structure studies of 3-(benzo[d][1,3]dioxol-5-yl)-5-(3-methylthiophen-2-yl)-4,5-dihydro-1H-pyrazole-1-carboxamide: Hirshfeld surface, DFT and thermal analysis, J. Mol. Struct. 1161 (2018) 285–298.

[37] A. Kawai, K. Obi, First observation of a radical-triplet pair mechanism (RTPM) with doublet precursor, J. Phys. Chem. 96 (1) (1992) 52–56.

[38] Z. Wang, J. Zhao, A. Barbon, A. Toffoletti, Y. Liu, Y. An, L. Xu, A. Karatay, H. G. Yaglioglu, E.A. Yildiz, M. Hayvali, Radical-enhanced intersystem crossing in new bodipy derivatives and application for efficient triplet-triplet annihilation upconversion, J. Am. Chem. Soc. 139 (23) (2017) 7831–7842.

[39] W.-L. Jiang, Z. Peng, B. Huang, X.-L. Zhao, D.Sun, X. Shi, and H.-B. Yang, TEMPO radical-functionalized supramolecular coordination complexes with controllable spin-spin.

[40] H. Zhang, B. Zhang, Y. Zhang, Z. Xu, H. Wu, P.-A. Yin, Z. Wang, Z. Zhao, D. Ma, B. Z. Tang, A multifunctional blue-emitting material designed via tuning distribution of hybridized excited-state for high-performance blue and host-sensitized OLEDs, Adv. Funct. Mater. 30 (2020) 2002323.